PNAS RESEARCH ARTICLE | CHEMISTRY

Manipulating ultrafast even-order nonlinear chiral responses of L-tryptophan by polarization pulse shaping

Jérémy R. Rouxel[a,1], Yeonsig Nam[a], Vladimir Y. Chernyak[b], and Shaul Mukamel[c,d,1]

Edited by Gregory S. Engel, The University of Chicago, Chicago, IL; received February 6, 2024; accepted April 23, 2024 by Editorial Board Member Peter J. Rossky

Molecular chirality has long been monitored in the frequency domain in the ultraviolet, visible, and infrared regimes. Recently developed time-domain approaches can detect time-dependent chiral dynamics by enhancing intrinsically weak chiral signals. Even-order nonlinear signals in chiral molecules have gained attention thanks to their existence in the electric dipole approximation, without relying on the weaker higher-order multipole interactions. We illustrate the optimization of temporal polarization pulse-shaping in various frequency ranges (infrared/optical and optical/X ray) to enhance chiral nonlinear signals. These signals can be recast as an overlap integral of matter and field pseudoscalars which contain the relevant chiral information. Simulations are carried out for second- and fourth-order nonlinear spectroscopies in L-tryptophan.

chirality | spectroscopy | pulse shaping | nonlinear optics | X-rays

Spectroscopic techniques for probing molecular chirality are undergoing rapid progress. Circular dichroism (CD), defined as the differential absorption of left and right circularly polarized light, is the most commonly used technique but provides a weak signal atop a stronger achiral background. Tang and Cohen (1, 2) have shown that CD signals are proportional to a quantity known as the "field chirality" introduced by Lipkin (3). This observation offers avenues to maximize intrinsically weak CD signals (4). Such optimization relies on matching the spatial profiles of the matter and field chiralities. Similar considerations can also be extended to the time-domain (5–7). Time-domain nonlinear techniques are very promising for the temporal optimization of ultrafast chiral signals because their multiple pulses offer the needed flexibility to match the field and matter chiral correlation functions. In all cases, the molecular chirality involves a pseudoscalar matter correlation function which depends on the chosen chiral-sensitive technique and that is probed by a corresponding probing field chiral correlation function (8).

Most nonlinear spectroscopic techniques, such as $\chi^{(3)}$ ones, are done with odd-order perturbative interactions in the incoming fields. The reason lies in the fact that even-order techniques vanish in centro-symmetric media (9). The sensitivity of even-order signals, such as sum-frequency generation (SFG), to parity breaking has long been used to probe interfaces (10, 11) and randomly oriented chiral molecules in the bulk of a liquid phase (12–15). However, when the matter is chiral, even-order techniques do not vanish in the electric dipole approximation, under some constraints on the incoming beams geometry, enabling strong chiral signals in the bulk (16–19). The rotationally averaged second-order $\chi^{(2)}$ signals can be factorized into two triple products: one of the three transition electric dipoles of matter given by $\boldsymbol{\mu}_{ab} \cdot \boldsymbol{\mu}_{cd} \times \boldsymbol{\mu}_{ef}$ and the three electric field polarizations for the incoming fields $\boldsymbol{E}_3 \cdot \boldsymbol{E}_2 \times \boldsymbol{E}_1$. These triple products are pseudoscalars that do not vanish only when the three vectors are noncoplanar. For chiral molecules, the absence of improper rotations guarantees it (20). For achiral molecules, the triple product vanishes by symmetry, and the leading contribution to $\chi^{(2)}$ has to include the electric quadrupole or the magnetic dipole (21). From the probing fields' perspective, this implies that the three interactions are achieved with noncoplanar fields. This is why SHG carried out with a single incoming beam vanishes even in chiral liquids. Note that the sign of the field pseudoscalar is determined by the handedness of the coordinate frame spawned by the three vector polarizations.

Various schemes have been developed for generating these pseudoscalar fields. Rentzepis et al. (12) have proposed the following frequency domain scheme to probe chiral liquids: beams with frequency ω and 2ω and crossed polarizations are generated and interact noncollinearly with a chiral sample. The SFG signal at frequency $\omega + 2\omega$ is finally homodyne-detected. This approach was employed by Belkin et al. (13, 22)

Significance

A molecule is chiral if it does not possess any plane of mirror symmetry. Chiral molecules are extremely important in drug synthesis, catalysis, and biochemistry, but spectroscopic signals characterizing them are usually weak. In this study, we show how even-order nonlinear techniques, such as sum-frequency generation, can be combined with polarization pulse shaping schemes to design sensitive probes of molecular chirality. Applications are made to an essential amino acid, L-tryptophan. The generality of this approach is demonstrated in various frequency regimes (optical and X-rays) and for different nonlinear interaction orders ($\chi^{(2)}$ and $\chi^{(4)}$ techniques).

Author affiliations: [a]Chemical Sciences and Engineering Division, Argonne National Laboratory, Lemont, IL 60439; [b]Wayne State University, Detroit, MI 48202; [c]Department of Chemistry, University of California, Irvine, CA 92697-2025; and [d]Department of Physics and Astronomy, University of California, Irvine, CA 92697-2025

Author contributions: J.R.R., V.Y.C., and S.M. designed research; J.R.R. and Y.N. performed research; J.R.R. analyzed data; and J.R.R., V.Y.C., and S.M. wrote the paper.

The authors declare no competing interest.

This article is a PNAS Direct Submission. G.S.E. is a guest editor invited by the Editorial Board.

[1] To whom correspondence may be addressed. Email: jrouxel@anl.gov or smukamel@uci.edu.

to probe limonene. They used optical and IR fields crossing at 90° at the sample. By scanning the IR frequency and measuring the SFG in reflection and transmission, they were able to separate bulk and interface contributions. The former is due to intrinsic molecular chirality while the latter is caused by symmetry breaking at the surface. Smirnova et al. (23–26) and Wörner et al. (27–29) have recently extended these approaches to High Harmonic Generation sources. They have used bicircular fields consisting of two counterrotating circularly polarized fields with frequencies ω and 2ω. Over the field period, the polarization forms a Lissajous pattern. Again, the combination of different polarizations and frequencies allows for the generation of a field pseudoscalar. It is a triple product at the lowest nonvanishing order, $\chi^{(2)}$, and can be generalized to higher orders (25). They have also extended the concept by ensuring that the field chirality is conserved spatially in the interaction region (24) so that the spatial handedness of the field polarization coordinates is preserved across the sample.

In this work, we demonstrate how sensitive even-order ultrafast chiral spectroscopies can be designed and optimized in chiral liquids and show how this maximization maps the molecular chiral correlation functions. We apply even-order $\chi^{(2)}$ and $\chi^{(4)}$ techniques to probe the UV-active amino acid L-tryptophan. Previous studies did not take advantage of the broad spectral envelope of ultrashort pulses to address multiple molecular eigenstates at once. We consider ultrashort pulses in the time domain with various levels of complexity, ranging from simple Gaussian pulses to temporally shaped pulses with polarization control. Applications are made to two types of SFG signals using low or high photon energy regimes: 1) $\chi^{(2)}$ IR + optical SFG, and 2) $\chi^{(2)}$ optical + X ray SFG schemes. Schemes (1) and (2) monitor the chirality of vibrational and electronic excited-states, respectively. Finally, we demonstrate how this approach can be extended to other techniques by discussing an example of a $\chi^{(4)}$ process. To that end, charge migration dynamics are calculated by starting with an actinic optical excitation followed by an optical + X-ray SFG process. We show how the temporal polarization profiles can be tuned to maximize the chiral response. Importantly, the chiral signal maximization signifies that the overlap between the field and matter chirality is increased and one is effectively mapping the matter chiral correlation function by tuning the field parameters. This tuning of the field chirality to maximize the signal is different from the one proposed by Tang and Cohen (2) which relied on the spatial variation of the field to maximize the field chirality at some well-defined locations. In contrast, our proposition tailors the temporal field polarization profiles to match the time-dependent molecular dipoles.

1. Probing Vibrations by Ground State SFG

We first present closed-form expressions for the SFG signals using pulses with arbitrary polarization and spectral profiles. These chiral-sensitive signals can be used to characterize molecular vibrational or electronic eigenstates in chiral molecules. SFG is a three-wave-mixing process induced by two incoming beams $\boldsymbol{E}_1$ and $\boldsymbol{E}_2$. The outgoing signal can be homodyne- or heterodyne-detected using a local oscillator $\boldsymbol{E}_{\mathrm{LO}}$ pulse. For even-order nonlinear techniques, the dominant light–matter coupling leading to the chiral response only involves the electric dipole (30):

$$H_{\mathrm{int}} = -\boldsymbol{\mu}\cdot\boldsymbol{E}(t), \qquad [1]$$

where $\boldsymbol{\mu}$ and $\boldsymbol{E}$ are the electric transition dipole operator and the incident electric fields respectively.

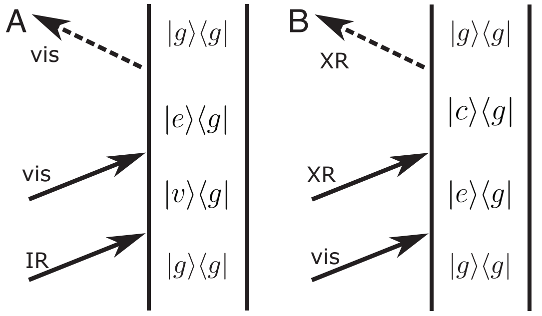

Fig. 1. Ladder diagrams for the SFG signals. (*A*) IR/optical and (*B*) optical/X-ray.

The SFG process can be represented by a ladder diagram representing an interaction pathway on the molecular density matrix (31). Both IR/optical, Fig. 1*A*, and optical/X-ray, Fig. 1*B* are considered in the following. Fig. 1*A* represents the commonly implemented SFG process with an initial IR interaction followed by an optical probe. Experiments which resolve vibrational modes at interfaces usually scan the IR beam central frequency, and the optical beam generates an easy-to-detect signal that is sensitive to parity breaking (32). Here, the lack of centrosymmetry is caused by molecular chirality in the bulk liquid, and not by the surface. These techniques use monochromatic light or narrowband pulses, and only spectral information is recorded.

The rotationally averaged frequency-dispersed heterodyne-detected SFG signal (Fig. 1 *A* or *B*) can be written as (8):

$$S^{(2)}_{\mathrm{SFG}}(\omega, T) = \frac{2}{\hbar^3}\frac{1}{6}\mathrm{Im}\int dt dt_2 dt_1 \epsilon_{ijk}\langle \mu_L^i \mathcal{G}(t_2)\mu_L^j \mathcal{G}(t_1)\mu_L^k\rangle \times \epsilon_{abc} E^{a*}_{\mathrm{LO}}(\omega) e^{i\omega t} E^b_2(t-t_2) E^c_1(t-t_2-t_1+T), \qquad [2]$$

where T is the delay between the IR and visible pulses, t_1 and t_2 are dummy variables which represent the perturbative expansion and $\mathcal{G}$ are field-free molecular propagators (31). The subscript L (R) on the dipoles stand for actions on the left (right) of the density matrix (31); see Fig. 1. The summation over repeated lower and higher indices is implied. The Levi-Civita contraction indicates a vector triple product $\epsilon_{ijk}u^i v^j w^k = \boldsymbol{u}\cdot(\boldsymbol{v}\times\boldsymbol{w})$ originating from the rotational averaging over molecular orientations. The triple products of the matter dipoles and of the electric field amplitudes are the rotational invariants of the third-rank matter response and of the field tensors, respectively.

Ultrashort measurements require pulses with a broad bandwidth. We shall recast the field amplitudes in the frequency domain:

$$\boldsymbol{E}^*_{\mathrm{LO}}(t) = \int \frac{d\omega_{\mathrm{LO}}}{2\pi} e^{i\omega_{\mathrm{LO}}t}\boldsymbol{E}^*_{\mathrm{LO}}(\omega_{\mathrm{LO}}), \qquad [3]$$

$$\boldsymbol{E}_2(t-t_2) = \int \frac{d\omega_2}{2\pi} e^{-i\omega_2(t-t_2)}\boldsymbol{E}_2(\omega_2), \qquad [4]$$

$$\boldsymbol{E}_1(t-t_2-t_1+T) = \int \frac{d\omega_1}{2\pi} e^{-i\omega_1(t-t_2-t_1+T)}\boldsymbol{E}_1(\omega_1). \qquad [5]$$

Eq. **2** then becomes:

$$S^{(2)}_{\mathrm{SFG}}(\omega, T) = \frac{2}{\hbar^3}\frac{1}{6}\mathrm{Im}\ \epsilon_{ijk}\epsilon_{abc}\int \frac{d\omega_2}{2\pi}\frac{d\omega_1}{2\pi}\delta(\omega-(\omega_2+\omega_1)) \langle \mu_L^i \mathcal{G}(\omega_2+\omega_1)\mu_L^j \mathcal{G}(\omega_1)\mu_L^k\rangle E^{a*}_{\mathrm{LO}}(\omega) E^b_2(\omega_2) E^c_1(\omega_1) e^{-i\omega_1 T}. \qquad [6]$$

The matter correlation function corresponding to Fig. 1*A* can be expanded in eigenstates:

$$\epsilon_{ijk}\langle \mu_L^i \mathcal{G}(\omega_2+\omega_1)\mu_L^j \mathcal{G}(\omega_1)\mu_L^k\rangle = \sum_{ev} \frac{\mu_{ge}\cdot(\mu_{ev}\times\mu_{vg})}{(\omega_2+\omega_1-\omega_{eg}+i\Gamma_{eg})(\omega_1-\omega_{vg}+i\Gamma_{vg})}. \qquad [7]$$

Eqs. **6** and **7** can be used to compute the SFG IR + visible signal. Before turning to numerical computations, we show in the next section how the signal can be recast as a matter/field overlap integral and how shaped field envelopes for various polarization components may be used to modify the chiral response.

2. Response to Polychromatic Chiral Fields

In recent works, the chiral fields pseudoscalars were constructed in the frequency domain by combination of a few monochromatic field modes (24, 28). While these have experimental advantages, they lack the generality to be resonant with a broad manifold of excited states.

To enhance the resonant time-domain probing, all pulses will be polarization-shaped. Pulses with nontrivial polarization states are represented in Fig. 2. When each polarization component of the fields is shaped in the time-domain, the probing field may be designed to maximize the field pseudoscalar, to maintain the sign of the field chirality in space, and to maximize their resonant interaction with the molecular states.

When limited to harmonics of the same source field, the field polarization runs through a Lissajous knot with parameters $(n_x, n_y, n_z) \in \mathbb{N}^3$. For example, for monochromatic fields, by crossing an elliptical field at frequency ω with a longitudinal component at 2ω, one gets the (1,1,2) knot.

$$\boldsymbol{E}(t) = \begin{pmatrix} E_\omega \cos\theta\cos(\omega t+\phi_x) \\ E_\omega \sin\theta\cos(\omega t+\phi_y) \\ E_{2\omega}\cos(2\omega t+\phi_z), \end{pmatrix} \qquad [8]$$

where the relative phases ϕ_x, ϕ_y, and ϕ_z of the various cartesian components determine the shape of the Lissajous knot (33).

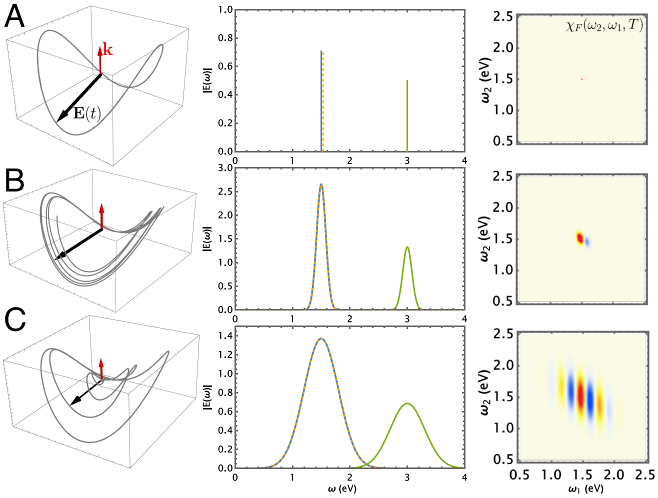

Fig. 2. *Left*: Light polarization trajectory in time domain. The red arrow represents the wavevector of the $\boldsymbol{E}_1$ and E_2 fields, and the black arrow is the polarization of the total field. *Center*: Spectral envelopes used for the three field components used in the SFG process. *Right*: Corresponding chiral field correlation function, Eq. **11** with $\omega = \omega_1 + \omega_2$. Three cases are considered: (*A*) Monochromatic fields, Eq. **8** ($E_\omega = 1$ au, $E_{2\omega} = 0.5$ au, $\omega = 1.5$ eV, $\theta = \pi/4$, $\alpha_x = 0.2$, $\alpha_y = \pi/2$, $\phi = 0.6$). (*B*) Narrowband fields centered at 1.5 eV (X,Y components) and 3 eV (Z component). (*C*) Broadband fields with the same central frequencies.

The polarization trajectory of this Lissajous knot pulse is displayed in Fig. 2*A* (*Left*). Since the beam is monochromatic (see corresponding spectra on the right), the polarization undergoes a periodic motion along the Lissajous knot.

Ultrashort pulses in time-resolved techniques must be broadband to achieve a high time resolution and to probe chiral dynamics involving multiple molecular eigenstates. We introduce the following polarization-shaped polychromatic fields:

$$\boldsymbol{E}_n(\omega) = \sum_{a=x,y,z}\sum_{\alpha} \boldsymbol{e}_a E_n^{a\alpha}(\omega-\omega_\alpha), \qquad [9]$$

where n indicates the nth pulse in the interaction pathway, a is the polarization component, and α runs over the basis used to generate the frequency profile. Each a component of the polarization is given by a sum of broadband contributions centered at frequencies ω_α. $E_n^{a\alpha}$ are typically Gaussian or Lorentzian field envelopes.

Fig. 2 *B* and *C* show examples of such fields given by:

$$\boldsymbol{E}(\omega) = \begin{pmatrix} E_x\, e^{-(\omega-\omega_x)^2/(2\sigma_x^2)} \\ E_y\, e^{-(\omega-\omega_y)^2/(2\sigma_y^2)} \\ E_z\, e^{-(\omega-\omega_z)^2/(2\sigma_z^2)} \end{pmatrix}, \qquad [10]$$

where $\omega_x = \omega_y = 1.5$ eV, $\omega_z = 3$ eV. In Fig. 2*B* the bandwidth σ are taken to be relatively narrow (0.08 eV) while in *C* they are broad (0.3 eV). For narrow bandwidths, the pulse durations are long and the polarization pattern is similar to the monochromatic case. For broad bandwidths, the polarization pattern becomes complex within a short period of time within the pulse.

We next introduce the field and matter chiral correlation functions for the SFG signals:

$$\chi_F^{(2)}(\omega,\omega_1,T) = \boldsymbol{E}^*_{\mathrm{LO}}(\omega)\cdot(\boldsymbol{E}_2(\omega-\omega_1)\times\boldsymbol{E}_1(\omega_1))e^{-i\omega_1 T}, \qquad [11]$$

$$\chi_M^{(2)}(\omega,\omega_1) = \sum_{ev}\frac{\boldsymbol{\mu}_{ge}\cdot(\boldsymbol{\mu}_{ev}\times\boldsymbol{\mu}_{vg})}{(\omega-\omega_{eg}+i\Gamma_{eg})(\omega_1-\omega_{vg}+i\Gamma_{vg})}. \qquad [12]$$

The chiral SFG signal can be finally recast as an overlap integral of these field and matter quantities:

$$S^{(2)}_{\mathrm{SFG}}(\omega,T) = \frac{2}{6\hbar^3}\mathrm{Im}\int\frac{d\omega_1}{2\pi}\chi_M^{(2)}(\omega,\omega_1)\chi_F^{(2)}(\omega,\omega_1,T). \qquad [13]$$

Maximizing the chiral signal amounts to optimizing the overlap of the above two field and matter chiral quantities. Reaching a maximum of the SFG chiral signal indicates that $\chi_F^{(2)}$ closely resemble $\chi_M^{(2)}$ and may thus be used to map the matter chiral correlation function.

Turning to the field chirality function $\chi_F^{(2)}(\omega_2,\omega_1,0)$ calculated for narrowband pulses, Fig. 2*B*, one can see that its sign is preserved over the entire spectral region of the pulses. Broadband pulses on the other hand produce a field pseudoscalar that changes sign over the spectral region, which can diminish the chiral-sensitivity of the signal when integrating over the pulse bandwidth. However, this should not be a limitation of broadband pulses, but rather provides a practical route for optimization. The field chirality itself can change sign for different transitions. Frequency-shaped pulses can then be engineered to closely match the matter chirality over the probed frequency range and during its dynamics. In this discussion and in Fig. 2, the field chiral response function is taken at $T = 0.5$ fs when the pulses $\boldsymbol{E}_1$ and $\boldsymbol{E}_2$ are almost coincident. In the following examples, when a sum-over-state expression with exponential phenomenological decays, the dynamics following the $\boldsymbol{E}_1$ pulses is trivial, and varying the delay T does not add extra information in the signal. It can however be used to control the phase of the field chiral correlation function to better match the matter chiral correlation function. In systems with nontrivial relaxation dynamics, the matter chiral response would depend on the delay T, and extra optimization steps can be made to maximize the field chirality at every step along the dynamics.

Eq. **13** assumes heterodyne detection. While this is customary for optical spectroscopic techniques, it remains a challenge for X-ray signals. In that case, the homodyne-detected signal may be preferred and is given by:

$$S^{(2)}_{\mathrm{SFG,hom}}(\omega, T) \propto \left| \int \frac{d\omega_1}{2\pi} \chi_M^{(2)}(\omega, \omega_1) \chi_F^{(2)}(\omega, \omega_1, T) \right|^2. \tag{14}$$

3. Applications to L-Tryptophan

3.1. Ab Initio Computation of the Electronic States. L-tryptophan is one of the three important UV-active amino acids (34) and is also a precursor for various important compounds such as serotonin or melatonin. Extended networks of tryptophan molecules have also been found to have remarkable optical properties (35). We use this molecule to illustrate polarization pulse shaping in even-order nonlinear spectroscopic signals.

The valence excitations were calculated using the multi-configurational self-consistent field (MCSCF) approach at the cc-pVDZ/SA5-CASSCF(8/6) level of theory with the MOLPRO package (36). Four valence-excited states were computed. The six orbitals considered ranged from HOMO-3 to LUMO+1. The resulting UV spectrum (transition frequencies and oscillator strengths) with a phenomenological broadening of 0.1 eV is displayed in Fig. 3*B*.

To calculate the C K-edge absorption spectrum, we used restricted active space core-excited states calculations (RASSCF) for each carbon 1s core molecular orbital. The second-order Douglas–Kroll–Hess Hamiltonian was used to account for relativistic corrections. The RASSCF calculations were performed at the cc-pVDZ/RASSCF(10/7) and two state-averaged core-excited states were calculated for each of the 11 carbon atoms in the L-tryptophan molecule. Note that the employed RASSCF method describes bound states and is thus adequate for the near-edge region of the X-ray spectrum, but not over the edge region where photoelectron scattering effects become predominant. Fig. 3*C* shows the stick absorption spectra with a 0.4 eV phenomenological broadening. Finally, the vibrational spectrum was computed by using the experimental data of Mohan et al. (37) The spectrum is displayed in Fig. 3*A* with a phenomenological broadening of 100 cm^{-1}.

3.2. IR/UV Sum-Frequency Generation. To illustrate how the polarization-shaped pulses can maximize the chiral signal over a broad range of excited states, it is instructive to compare the chiral matter correlation functions, Eq. **12**, and the field, Eq. **11**. To demonstrate the impact of polarization pulse shaping on the chiral $\chi^{(2)}$ SFG signal, we display these two correlation functions for the IR/UV signals in Fig. 4.

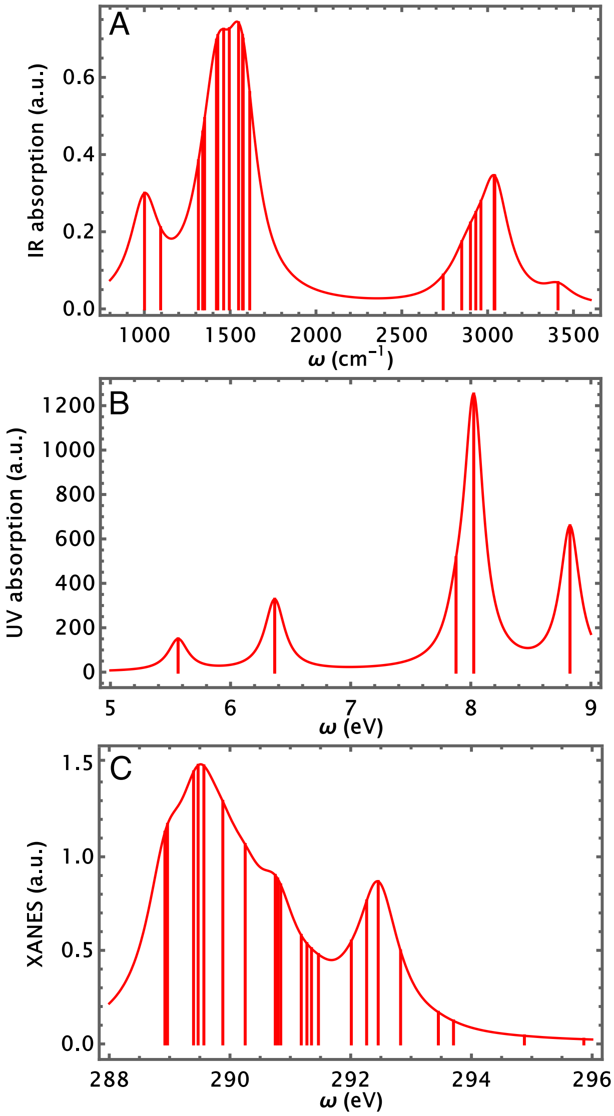

Fig. 3. Computed L-tryptophan linear absorption spectra covering (*A*) vibrational, (*B*) valence, and (*C*) carbon K-edge core excitations.

The IR/UV matter chiral response $\chi_M^{(2)}(\omega, \omega_1)$ displayed in Fig. 4*A* is a purely molecular property that fully describes the chiral response in the studied frequency regime for this chirality-sensitive technique. In panels 4*B* and 4*C*, two different field chiral correlation functions $\chi_F^{(2)}(\omega, \omega_1, T)$ are employed to probe $\chi_M^{(2)}(\omega, \omega_1)$. The polarizations were chosen to be orthogonal: $\boldsymbol{e}_{\mathrm{LO}} = (0, 0, 1)$, $\boldsymbol{e}_2 = (1, 0, 1)$ and $\boldsymbol{e}_1 = (0, 1, 0)$. This greatly simplifies the polarization triple product computation. In more realistic experimental geometries, one would have to consider a set of convenient pulse wavevectors with noncoplanar polarizations at the sample location. The triple product would then be obtained by simple geometric calculations.

In the following examples, we have considered coincident pulses (T = 0). Varying this delay would allow for further optimization of the field pseudoscalar or the further study of molecular dynamics occurring during that delay.

The first configuration, whose chiral field correlation function is displayed in Fig. 4*B*, has a single Gaussian for each of the three

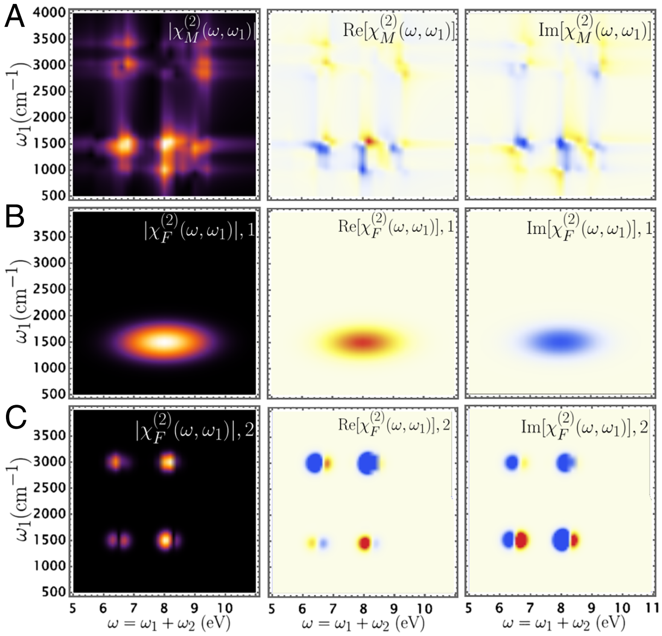

Fig. 4. Chiral correlation functions probed by IR/UV SFG signals. (*A*) Matter chiral correlation function $\chi_M^{(2)}(\omega,\omega_1)$. (*B*) Field chiral correlation function $\chi_F^{(2)}(\omega,\omega_1,T=0)$ for a single Gaussian pulse for each incoming field. The field parameters are chosen as follows: $E_1 = E_2 = E_{\mathrm{LO}} = 1$ au, $\omega_1 = 1{,}500$ cm^{-1}, $\sigma_1 = 200$ cm^{-1}, $\omega_2 = 7.81$ eV, $\sigma_2 = 1.$ eV, $\omega_{\mathrm{LO}} = 8$ eV, $\sigma_{\mathrm{LO}} = 1.5$ eV. (*C*) Same as *B* but with multiple Gaussian envelopes for each pulse. The field parameters are chosen as follow: $E_{1a} = E_{1b} = 1$ au, $\omega_{1a} = 1{,}500$ cm^{-1}, $\omega_{1b} = 3{,}000$ cm^{-1} and $\sigma_{1a} = \sigma_{1b} = 100$ cm^{-1}. $E_{2a} = E_{2c} = -E_{2b} = -E_{2d} = 1$ au, $\omega_{2a} = 8.2$ eV, $\omega_{2b} = 8$ eV, $\omega_{2c} = 6.4$ eV, $\omega_{2d} = 6.2$ eV, $\sigma_{2a} = \sigma_{2b} = 0.3$ eV, $\sigma_{2c} = 0.4$ eV, $\sigma_{2d} = 0.4$ eV. $E_{\mathrm{LO},a} = E_{\mathrm{LO},b} = 1$ au, $\omega_{\mathrm{LO},a} = 8.1$ eV, $\omega_{\mathrm{LO},b} = 6.3$ eV, $\sigma_{\mathrm{LO},a} = \sigma_{\mathrm{LO},b} = 0.2$ eV.

pulses $\boldsymbol{E}_1, \boldsymbol{E}_2$, and $\boldsymbol{E}_{\mathrm{LO}}$. This corresponds to a loose overlap between $\chi_M^{(2)}(\omega,\omega_1)$ and $\chi_F^{(2)}(\omega,\omega_1,T)$ for that spectral region. This pulse configuration thus allows to probe the IR/UV SFG signal, but is not optimized to closely fit $\chi_M(\omega,\omega_1)$ in that region. In Fig. 4*B*, the IR field resonant with the C–C stretching band at 1,427 and 1,555 cm^{-1}. The UV pulse is centered at 8 eV, matching the strongest oscillator strength in Fig. 3*A*.

In Fig. 4*C*, shaped pulses constructed as the sum of several Gaussian envelopes are employed to build a field pseudoscalar with a larger spectral overlap with the matter one. This allows resonances with both the C–C stretching and the C–H stretching in the 2,849 to 3,042 cm^{-1} region by using two Gaussians (centered at 1,500 and 3,000 cm^{-1}) for the IR pulse. Four Gaussians for the UV pulse (centered at 6.2, 6.4, 8, and 8.22 eV) allow for resonances with multiple electronic excitations. We have retained a reasonably simple pulse spectral profile for each of the $\boldsymbol{E}_1, \boldsymbol{E}_2$, and $\boldsymbol{E}_{\mathrm{LO}}$ pulses, while improving the overlap with the chiral matter correlation function. Pulses intensities were normalized to unity to ensure that signals with equivalent incoming photon fluxes are compared.

The SFG signals probed with these two pulse configurations are displayed in Fig. 5 *A* and *B*. These signals are given by overlap integrals of the matter and field chiral correlation function in the frequency domain, Eq. **2**. The aim of the polarization pulse shaping is to bring the field chiral correlation function as close as possible to the matter chiral correlation function in order to maximize the chiral response, Eq. **13**. The pulse configuration leading to the signal displayed in Fig. 5*B* matches more closely the matter chiral correlation function, and thus resulting in a larger signal in absolute amplitude (about 50% larger for the 8 eV spectral feature). This is a results of the field correlation in Fig. 7*C* having spectral features in the ($\omega = 8\mathrm{eV}, \omega_1 = 1{,}500$ cm^{-1}) and the ($\omega = 6\mathrm{eV}, \omega_1 = 1{,}500$ cm^{-1}) ranges where the matter correlation function is displaying a similar spectral behavior. The configuration used to get Fig. 7*C* remains relatively simple. More elaborate spectral and polarization shaping has the potential to further increase the signals.

3.3. UV/X-Ray Sum-Frequency Generation. We now turn to the analogous UV/X-ray SFG signals. While the vibrational manifold is probed by using an optical pulse as a window in Fig. 1 *A* and *B* presents a higher energy extension of this technique in which the valence excited-state manifold is probed by an X-ray pulse. This is reminiscent of the recently proposed stimulated X-ray Raman process (38, 39), in which a broadband X-ray pulse probes many valence excitation simultaneously. While nonlinear X-ray spectroscopies are still in their infancies (40, 41), multiple pulse (42, 43) and polarization-control (44, 45) schemes are being developed. Ultrafast even-order nonlinear spectroscopies should be available in the near future at X-ray facilities, and a partial optimization of chiral signals should then become possible.

The implementation of UV and X-ray three-wave-mixing signals is still in its infancy (46–49). Such signals would offer additional structural information compared to their lower energy counterparts. The chiral matter correlation function for UV + X-ray SFG in L-tryptophan is displayed in Fig. 7*A*. From Fig. 1*B*, the signal expression remains the same (Eq. **13**), but with the matter correlation function replaced by:

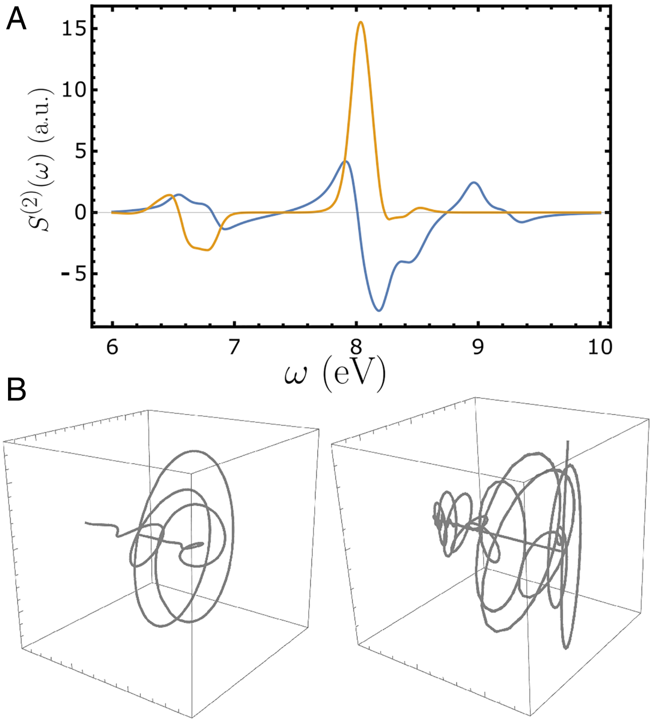

Fig. 5. (*A*) IR/UV chiral SFG signals, Eq. **13**, calculated for the pulse configurations displayed in Fig. 4 *B* and *C* (in blue and orange respectively). (*B*) Corresponding total incoming field polarization temporal profiles (*Left*: Fig. 4 *B*, *Right*: Fig. 4*C*).

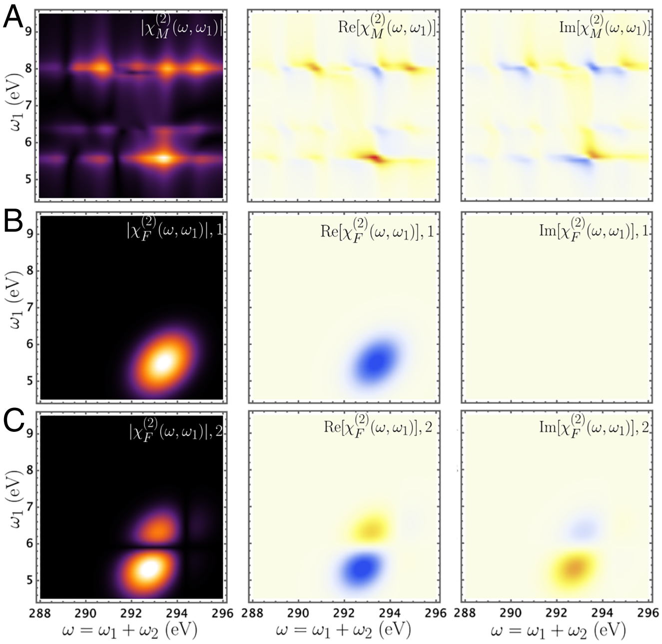

Fig. 6. Chiral correlation functions probed by UV/X-ray SFG signals. (*A*) L-tryptophan chiral correlation function $\chi_M(\omega, \omega_1)$. (*B*) Field chiral correlation function computed with the following parameters: $\omega_1 = 5.5$ eV, $\omega_2 = 287.9$ eV, $\omega_{\mathrm{LO}} = 293.4$ eV, $\sigma_1 = 0.5$ eV, $\sigma_2 = \sigma_{\mathrm{LO}} = 1.$ eV, $E_1 = E_2 = E_{\mathrm{LO}} = 1$ au. (*C*) Field chiral correlation function computed with polychromatic chiral fields using the following parameters for $\boldsymbol{E}_1$ ($\omega_{1a} = 5.5$ eV, $\omega_{1b} = 6.1$ eV, $\sigma_{1a} = \sigma_{1b} = 0.5$ eV, $E_{1a} = 1$ a.u., $E_{1ba} = -0.75$ a.u.), for $\boldsymbol{E}_2$ ($\omega_{2a} = 287.6$ eV, $\omega_{2a} = 287.2$ eV, $\sigma_{2a} = \sigma_{2b} = 1$ eV, $E_{1a} = 1$ a.u., $E_{1ba} = 1.9$ a.u.), for $\boldsymbol{E}_{\mathrm{LO}}$ ($\omega_{\mathrm{LO},a} = 293.1$ eV, $\omega_{\mathrm{LO},b} = 294$ eV, $\sigma_{\mathrm{LO},a} = \sigma_{\mathrm{LO},b} = 1$ eV, $E_{\mathrm{LO},a} = 1$ a.u., $E_{\mathrm{LO},b} = 0.5$ a.u.). Pulse energies are normalized.

$$\chi_M^{(2)}(\omega, \omega_1) = \sum_{ce} \frac{\mu_{gc} \cdot (\mu_{ce} \times \mu_{eg})}{(\omega - \omega_{cg} + i\Gamma_{cg})(\omega_1 - \omega_{eg} + i\Gamma_{eg})}, \quad \textbf{[15]}$$

where e and c label the valence- and core-excited states, respectively.

As done above, two field chiral correlation functions are considered. As for the IR/UV SFG, the first configuration considered is constructed from a single Gaussian envelope for each of the pulses. The corresponding chiral field correlation function and parameter is shown in Fig. 7*B*. For the second field configuration, displayed in Fig. 7*C*, each pulse is built by a sum of two Gaussian pulses. The UV/X-ray SFG signals are finally displayed in Fig. 6 *A* and *B*. Similar to the IR/UV case, the amplitude of the signal with an improved beam configuration in Fig. 6*B* is larger than when a single Gaussian pulse is used in Fig. 6*A*. The use of shaped pulses increases the signal amplitude by 2 compared to simple Gaussian pulses. The frequency-dispersed local oscillator allows targeting a desired spectral feature, while frequency-integrated signals could take advantage of a better overlap between field and matter chiral pseudoscalars over a broader spectral range. The latter strategy can provide a larger chiral signal enhancement but requires more complex temporal polarization profiles than can be achieved using optimal control feedback loop (50).

3.4. Probing Excited-State Charge Migration by Time-Domain $\chi^{(4)}$.

The ultrafast SFG process discussed above starts with a molecule in its electronic ground state. The spectral profiles can be shaped with various degrees of complexity to maximize the overlap between the field and the matter chiral correlation functions. These concepts are quite general and can be applied to molecules experiencing electronic or nuclear dynamics. As an example, we now turn to a $\chi^{(4)}$ signal, in which the first two interactions correspond to an actinic excitation that induces a charge migration in the L-tryptophan molecule. The process is then probed by a UV + X-ray SFG signal after a delay T. As higher-order signals are considered, the number of pulse parameters and matter transition dipoles involved is increased. Note that this $\chi^{(4)}$ is actually a second-order process with respect to the probe pulses.

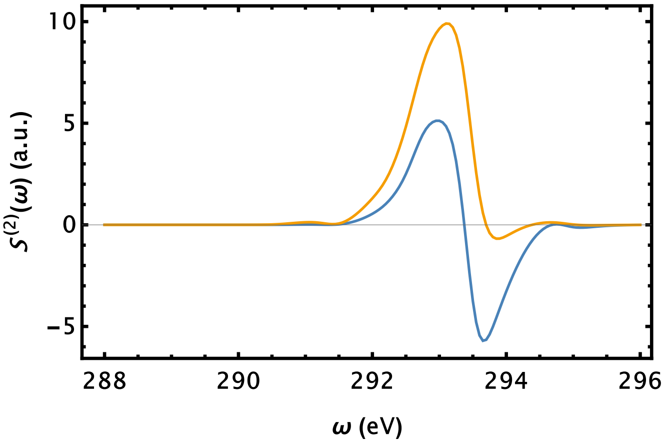

Fig. 7. UV/X-ray chiral SFG signals, Eq. **13**, calculated for the pulse configurations displayed in Fig. 7 and c (in blue and orange, respectively). The second pulse configuration has been selected to maximize the feature at 293 eV.

To simplify the discussion, we consider a pulse configuration in which only two interaction pathways are resonant and obey the phase-matching condition, as shown in the diagrams of Fig. 8. The two interactions with the actinic pump pulse $\boldsymbol{E}_{\mathrm{p}}$ are denoted by the label p and leave the molecule in a $|e\rangle\langle e'|$ coherence. Then, the pulses $\boldsymbol{E}_{\mathrm{v}}$, $\boldsymbol{E}_{\mathrm{x}}$, and $\boldsymbol{E}_{\mathrm{LO}}$ achieve the UV + X-ray process. $\boldsymbol{E}_{\mathrm{LO}}$ is the local oscillator that has a central frequency in the X-ray regime.

The signal involves five-point correlation functions given by a sum over the diagrams in Fig. 8 *A* and *B*:

$$S^{(4)}(\omega, T) = \sum_{\alpha=a,b} S_\alpha^{(4)}(\omega, T), \quad \textbf{[16]}$$

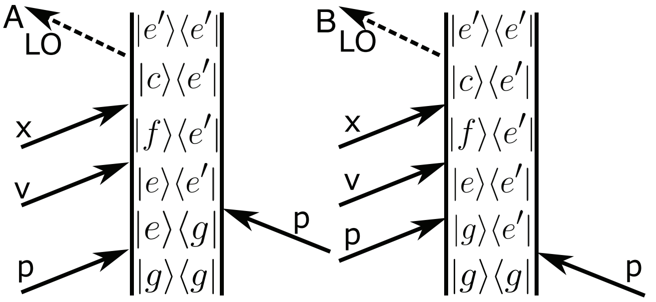

Fig. 8. Ladder diagrams for $\chi^{(4)}$ signals, Eq. **16**. These diagrams represent an SFG process starting from an electronic excited state population or coherence. Diagrams (*A*) and (*B*) correspond to the IR+optical and the optical+X-ray techniques, respectively.

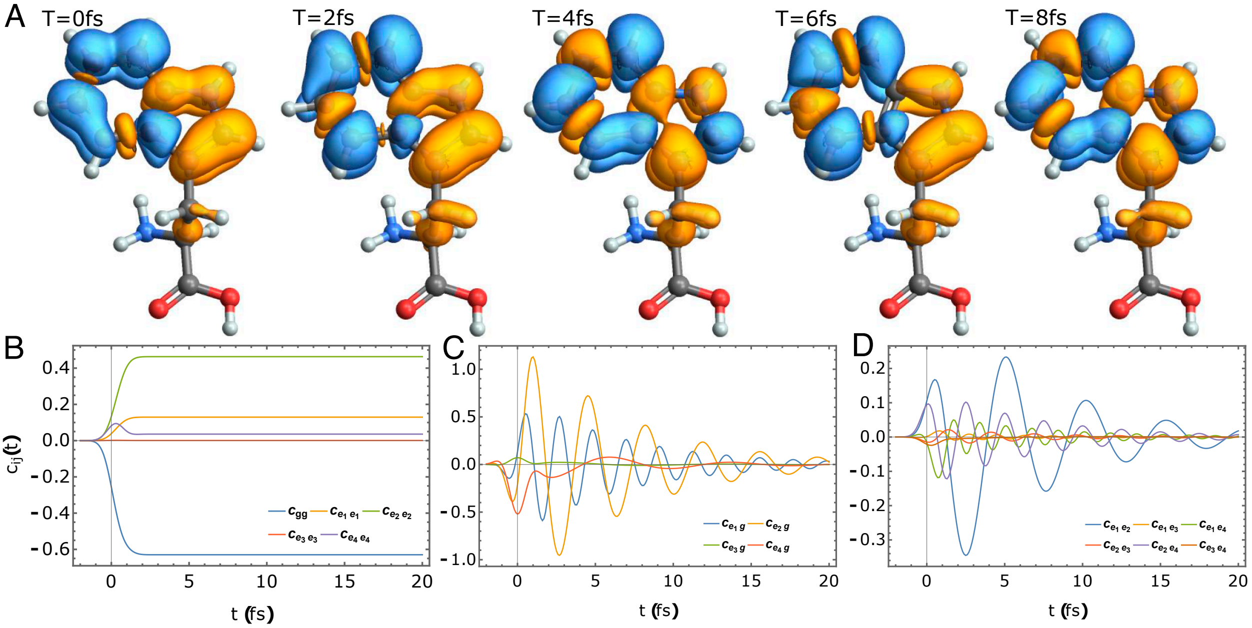

Fig. 9. Charge migration in L-tryptophan triggered by a Gaussian pump pulse E_p with central frequency $\omega_\mathrm{p} = 6$ eV and spectral bandwidth $\sigma_\mathrm{p} = 0.9$ eV. (*A*) Isosurfaces representing the difference charge density $\langle\sigma(r,T)\rangle - \langle\sigma(r,0)\rangle$. (*B–D*) represent the time evolution coefficients of the populations c_{ee}, ground to valence coherence c_{eg}, and excited state contributions respectively; see Appendix 5.1.

where α indicates the two diagrams in Fig. 8. The multipoint correlation functions associated to $S_a^{(4)}(\omega, T)$ and $S_b^{(4)}(\omega, T)$ are detailed in Appendix 5.3. The signal can be recast as sum of overlap integrals over the interaction pathways:

$$S^{(4)}(\omega, T) = -\frac{2}{30\hbar^5}\mathrm{Im}\int \frac{d\omega_4}{2\pi}\dots\frac{d\omega_1}{2\pi} \times \sum_\alpha \chi_M^{(4,\alpha),ijklm}(\omega_4,\omega_3,\omega_2,\omega_1) I^{(5)}_{ijklm,abcde} \times \chi_F^{(4,\alpha),abcde}(\omega, T; \omega_4,\omega_3,\omega_2,\omega_1), \quad [17]$$

where the field and matter chiral response functions are given in Appendix 5.3.

Formally, the signal in Eq. **17** is similar to the one given in Eq. **13** but involves additional pulses that can be shaped to maximize the overlap integral. Here, we restrict the discussion to a simple case in which each pulse is Gaussian with the following central frequencies: $\omega_\mathrm{p} = 6$ eV, $\omega_\mathrm{v} = 2$ eV, $\omega_\mathrm{x} = 280.9$ eV, and $\omega_\mathrm{LO} = 288$ eV. The spectral bandwidths are chosen to be $\sigma_\mathrm{p} = 0.9$ eV, $\sigma_\mathrm{v} = 0.3$ eV, $\sigma_\mathrm{x} = 2$ eV, and $\sigma_\mathrm{LO} = 2$ eV. The electronic dynamics triggered by the pump pulse E_p leads to the charge migration displayed in Fig. 9. Charge migration has been the focus of multiple studies recently (51–54). These studies often focus on the charge migration following a sudden ionization. Here, we consider a charge migration perturbatively driven by a UV actinic pulse. The charge density dynamics is displayed in Fig. 9*A*. The time-evolving charge density is obtained as sum-over-states using the density matrix perturbed up to second-order in the UV pulse. The corresponding coefficients are displayed in Fig. 9 *B–D* and their expressions are detailed in Appendix 5.1. The electronic dynamics is mostly localized in the tryptophan aromatic ring and behaves like a ring current (55). In aromatic achiral compounds, ring currents could be created by a circularly polarized actinic pulse and $S^{(4)}(\omega, T)$ could be a sensitive probe.

The molecule evolves freely for a delay T and is finally probed by the coincident $\boldsymbol{E}_\mathrm{v}$, $\boldsymbol{E}_\mathrm{x}$, and $\boldsymbol{E}_\mathrm{LO}$ pulses. The resulting $S^{(4)}(\omega, T)$ is displayed in Fig. 10*A*. The beating between the coherence $|e_1\rangle\langle g|$, $|e_2\rangle\langle g|$ and $|e_2\rangle\langle e_1|$ can be observed by the change in relative intensities of the peaks in the 286 to 288 eV region.

4. Conclusions

The use of broadband polarization-shaped pulses offers numerous opportunities to 1) maximize a given chiral-sensitive signal and 2) characterize the matter chiral correlation function. Even-order nonlinear spectroscopic techniques are excellent candidates for this approach because they already possess strong sensitivity to molecular chirality. The absence of higher-order multipoles guarantees that the signals are not buried under a strong achiral background. To design such signals, it is imperative to generate a field pseudoscalar from the field correlation function, which is only possible if the different field polarizations are not coplanar. For ultrashort pulses, this field pseudoscalar depends on the frequency variables and does not necessarily match the matter chiral response. This can potentially erode the chiral response when multiple eigenstates are contributing to the signal, which is typically the case when broadband ultrashort pulses are used. Pulse shaping offers a promising way to overcome this issue by maximizing the chiral response. This is achieved by closely matching the field and matter chiralities in the time domain. Alternatively, if the system eigenstates are not known, an experimental maximization of the chiral nonlinear signals via an optimization learning protocol would allow to map the chiral molecular correlation function.

While three-wave-mixing spectroscopies have been carried out for decades in the optical regime (12), five-wave-mixing experiments in chiral ensemble are less common. Nonetheless, they have been demonstrated to be achievable and sensitive to molecular chirality (56–59). The present approach is applicable

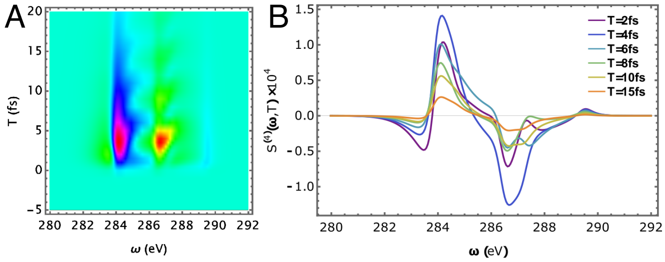

Fig. 10. (*A*) $S^{(4)}(\omega,T)$ signal, Eq. **17**, monitoring the charge migration in L-tryptophan displayed in Fig. 9. (*B*) Slices of $S^{(4)}(\omega,T)$ are fixed delays T.

to most chiral-sensitive spectroscopies, as long as they can be recast as a product of field and matter chiral pseudoscalars.

The proposed schemes can be implemented in the optical regime using recent progress in polarization pulse shaping (60–62). In the infrared, a careful design of the pulses and sample geometry is required to avoid potential artifacts (63). The temporal control of polarization usually relies on two-layer spatial light modulators (60) to shape independently orthogonal polarization component of a single ultrashort pulse. Intricate polarization profiles have been designed to optimize the ionization yield of a diatomic molecule (61). In the X-ray regime, the control of pulses polarization is more challenging, but recent demonstrations are showing the feasibility of polarization pulse shaping at seeded FELs (64).

Future directions will include the implementation of closed-loop pulse shaping approaches in which the spectral profile of each incoming polarization component is varied with the maximization of the nonlinear signals as an optimization target. Extensions in the context of nontrivial dynamics involving realistic relaxation models or nuclear dynamics are also an exciting avenue. Finally, the mapping of the molecular chiral correlation functions associated with various techniques provides a wealth of spectroscopic information. Applications to different molecular systems will allow determining how structural and dynamical insights can be gained from optimized ultrafast chiral techniques.

5. Materials and Methods

5.1. Perturbative Description of Charge Migration. Charge migration following the actinic pulse discussed in Section 3.4 is treated perturbatively at the second order. The motion of charge within the molecule is defined as the difference of charge densities of the photoexcited and ground state molecule:

$$\Delta\sigma(\mathbf{r},t)=\langle\sigma(\mathbf{r},t)\rangle-\langle\sigma(\mathbf{r},0)\rangle, \qquad [18]$$

where $\langle\sigma(\mathbf{r},0)\rangle=\sigma_{gg}(\mathbf{r})$ and

$$\langle\sigma(\mathbf{r},t)\rangle=\mathrm{Tr}\Big[\sigma(\mathbf{r})\rho(t)\Big]=\sum_{ee'}\rho_{e'e}(t)\sigma_{ee'}(\mathbf{r}). \qquad [19]$$

The interaction pathways in Liouville space contributing to the charge density expectation value up to second order in the incoming field are displayed in Fig. 11.

Since the charge densities matrix elements are symmetric $\sigma_{ee'}(\mathbf{r})=\sigma_{e'e}(\mathbf{r})$, the density matrix can be summed over symmetric pairs to use only real coefficients. For example, for the first-order perturbation terms, we have:

$$\rho^{(1)}_{eg}(t)\sigma_{ge}(\mathbf{r})+\rho^{(1)}_{ge}(t)\sigma_{eg}(\mathbf{r})=(\rho^{(1)}_{eg}(t)+\rho^{(1)}_{ge}(t))\sigma_{eg}(\mathbf{r})=c_{eg}(t)\sigma_{eg}(\mathbf{r}), \qquad [20]$$

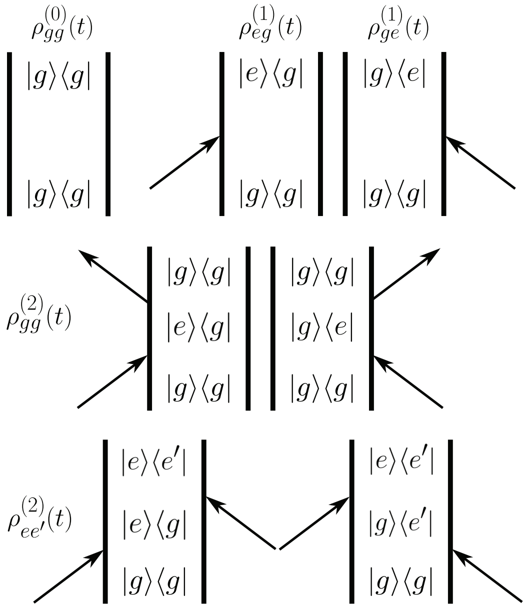

Fig. 11. Ladder diagram for the density matrix elements up to a second-order perturbation in the actinic field, triggering a charge migration.

where we have defined $c_{eg}(t)=\rho^{(1)}_{eg}(t)+\rho^{(1)}_{ge}(t)=2\mathrm{Re}(\rho^{(1)}_{eg}(t))$. The perturbative expansion of the charge density difference is then given by:

$$\Delta\sigma(\mathbf{r},t)=c_{gg}(t)\sigma_{gg}(\mathbf{r})+\sum_e c_{eg}(t)\sigma_{eg}(\mathbf{r})+\sum_e c_{ee}(t)\sigma_{ee}(\mathbf{r}) + \sum_{\substack{ee'\\ e>2,e'>e}} c_{ee'}(t)\sigma_{ee'}(\mathbf{r}), \qquad [21]$$

where we have explicitly separated the second-order ground state contribution, the first-order ground to valence coherence (*eg*) contribution, and the second-order population (*ee*) and coherence (*ee*′) contributions in the valence excited states.

We now provide explicit expressions for the density matrix elements:

$$\rho^{(1)}_{eg}(t)=\Big(-\frac{i}{\hbar}\Big)\int_0^{+\infty}dt_1\Big(-\boldsymbol{\mu}_{eg}\cdot\mathbf{E}(t-t_1)\Big)e^{-i\omega_{eg}t_1-\Gamma_{eg}t_1}, \qquad [22]$$

$$\rho^{(2)}_{gg}(t)=2\mathrm{Re}\Big(-\frac{i}{\hbar}\Big)^2\sum_e\int_0^{+\infty}dt_2dt_1\,\boldsymbol{\mu}_{eg}\cdot\mathbf{E}^*(t-t_2)\times\boldsymbol{\mu}_{eg}\cdot\mathbf{E}(t-t_2-t_1)e^{-i\omega_{eg}t_1-\Gamma_{eg}t_1}, \qquad [23]$$

$$\rho^{(2)}_{ee}(t)=-2\mathrm{Re}\Big(-\frac{i}{\hbar}\Big)^2\sum_e\int_0^{+\infty}dt_2dt_1\Big(\boldsymbol{\mu}_{eg}\cdot\mathbf{E}^*(t-t_2)\Big)\times\Big(\boldsymbol{\mu}_{eg}\cdot\mathbf{E}(t-t_2-t_1)\Big)e^{-i\omega_{eg}t_1-\Gamma_{eg}t_1}e^{-\Gamma_{ee}t_2}, \qquad [24]$$

$$\rho^{(2)}_{ee',e\neq e'}(t)=-\Big(-\frac{i}{\hbar}\Big)^2\sum_e\int_0^{+\infty}dt_2dt_1\Big[\boldsymbol{\mu}_{e'g}\cdot\mathbf{E}^*(t-t_2)\,\boldsymbol{\mu}_{eg}\cdot\mathbf{E}(t-t_2-t_1)e^{-i\omega_{eg}t_1-\Gamma_{eg}t_1}e^{-i\omega_{ee'}t_2-\Gamma_{ee'}t_2} + \boldsymbol{\mu}_{eg}\cdot\mathbf{E}(t-t_2)\,\boldsymbol{\mu}_{e'g}\cdot\mathbf{E}^*(t-t_2-t_1)e^{i\omega_{e'g}t_1-\Gamma_{e'g}t_1}e^{-i\omega_{ee'}t_2-\Gamma_{ee'}t_2}\Big]. \qquad [25]$$

In the main text, the pump pulse is assumed to have Gaussian envelope in the frequency domain. Its expression and corresponding temporal profile are given by:

$$\boldsymbol{E}(\omega) = \boldsymbol{E}\, e^{-\frac{(\omega-\omega_p)^2}{2\sigma_p^2}}, \quad [26]$$

$$\boldsymbol{E}(t) = \boldsymbol{E}\frac{\sigma}{\sqrt{2\pi}} e^{-\frac{\sigma^2}{2}t^2} e^{-i\omega_p t}. \quad [27]$$

Finally, the c coefficients for the charge migration treated perturbatively at second order are given by:

$$c_{eg}(t) = -\frac{2}{\hbar}\frac{\sigma_p}{\sqrt{2\pi}}\boldsymbol{\mu}_{eg}\cdot\boldsymbol{E}\,\mathrm{Re}\int_0^{+\infty} dt_1\, e^{-\frac{\sigma_p^2}{2}(t-t_1)^2} e^{i(\omega_p-\omega_{eg}+i\Gamma_{eg})t_1} e^{-i\omega_p t}, \quad [28]$$

$$c_{gg}(t) = -\frac{\sigma_p^2}{\pi\hbar^2}\sum_e |\boldsymbol{\mu}_{eg}\cdot\boldsymbol{E}|^2\mathrm{Re}\int_0^{+\infty} dt_2 dt_1\, e^{-\frac{\sigma_p^2}{2}(t-t_2)^2} e^{-\frac{\sigma_p^2}{2}(t-t_2-t_1)^2} e^{i(\omega_p-\omega_{eg}+i\Gamma_{eg})t_1}, \quad [29]$$

$$c_{ee}(t) = \frac{\sigma_p^2}{\pi\hbar^2}|\boldsymbol{\mu}_{eg}\cdot\boldsymbol{E}|^2\mathrm{Re}\int_0^{+\infty} dt_2 dt_1\, e^{-\frac{\sigma_p^2}{2}(t-t_2)^2} e^{-\frac{\sigma_p^2}{2}(t-t_2-t_1)^2} e^{i(\omega_p-\omega_{eg}+i\Gamma_{eg})t_1} e^{-\Gamma_{ee}t_2}, \quad [30]$$

$$c_{ee'}(t) = \frac{\sigma_p^2}{\pi\hbar^2}\boldsymbol{\mu}_{eg}\cdot\boldsymbol{E}\,\boldsymbol{\mu}_{e'g}\cdot\boldsymbol{E}\,\mathrm{Re}\int_0^{+\infty} dt_2 dt_1 e^{-\frac{\sigma_p^2}{2}(t-t_2)^2} e^{-\frac{\sigma_p^2}{2}(t-t_2-t_1)^2} e^{-i\omega_{ee'}t_2-\Gamma_{ee'}t_2} (e^{i(\omega_p-\omega_{eg}+i\Gamma_{eg})t_1} + e^{i(-\omega_p-\omega_{e'g}-i\Gamma_{e'g})t_1}). \quad [31]$$

5.2. The Lineshape Function. When using broadband Gaussian pulses or shaped pulses made of multiple Gaussian pulses, the following integral appears repeatedly in the signal expressions:

$$I = \int_{-\infty}^{-\infty}\frac{d\omega}{2\pi} e^{-\frac{(\omega-\bar{\omega})^2}{2\sigma^2}}\frac{e^{-i\omega t}}{\omega-\omega_{eg}+i\Gamma_{eg}}. \quad [32]$$

This integral can be calculated as follows:

$$I = \mathrm{FT}^{-1}\Big[e^{-\frac{(\omega-\bar{\omega})^2}{2\sigma^2}}\frac{1}{\omega-\omega_{eg}+i\Gamma_{eg}}\Big](t) \quad [33]$$

$$= \mathrm{FT}^{-1}\Big[e^{-\frac{(\omega-\bar{\omega})^2}{2\sigma^2}}\Big] * \mathrm{FT}^{-1}\Big[\frac{1}{\omega-\omega_{eg}+i\Gamma_{eg}}\Big](t) \quad [34]$$

$$= \Big[\frac{\sigma}{\sqrt{2\pi}}e^{-\frac{\sigma^2}{2}\tau^2}e^{-i\bar{\omega}\tau}\Big] * \Big[-i\theta(\tau)e^{-i\omega_{eg}\tau-\Gamma_{eg}\tau}\Big](t) \quad [35]$$

$$= -i\frac{\sigma}{\sqrt{2\pi}}\int_{-\infty}^{-\infty} d\tau\,\theta(t-\tau)e^{-\frac{\sigma^2}{2}\tau^2}e^{-i\bar{\omega}\tau}e^{-i\omega_{eg}(t-\tau)-\Gamma_{eg}(t-\tau)}, \quad [36]$$

where FT^{-1} stands for the inverse Fourier transform, $*$ for the convolution product and $\theta(\tau)$ is the Heaviside function. Finally, the last expression can be carried out analytically and gives:

$$I = -\frac{i}{2}e^{-i\omega_{eg}t-\Gamma_{eg}t}e^{\frac{1}{2\sigma^2}(\Gamma_{eg}+i(\omega_{eg}-\bar{\omega}))^2} \mathrm{erfc}\Big(\frac{\Gamma_{eg}-\sigma^2 t+i(\omega_{eg}-\bar{\omega})}{\sqrt{2}\sigma}\Big). \quad [37]$$

This last expression can be used to compute efficiently signals presented in the article. Even when multidimensional integrals are required, for example for $\chi^{(4)}$ signals, numerical evaluations on a grid can be simplified by carrying one of the integrals analytically with this result.

5.3. Contributions to $\boldsymbol{S^{(4)}(\omega, T)}$. The two contributions are given by:

$$S_a^{(4)}(\omega,T) = -\frac{2}{\hbar^5}\mathrm{Im}\int\frac{d\omega_4}{2\pi}\frac{d\omega_3}{2\pi}\frac{d\omega_2}{2\pi}\frac{d\omega_1}{2\pi} \delta(\omega-\omega_4-\omega_3+\omega_2-\omega_1)I^{(5)}_{ijklm,abcde}E^{a*}_{\mathrm{LO}}(\omega)E^b_{\mathrm{x}}(\omega_4)E^c_{\mathrm{v}}(\omega_3) E^{d,*}_{\mathrm{p}}(\omega_2)E^e_{\mathrm{p}}(\omega_1)e^{i(\omega_2-\omega_1)T}\times\langle\mu^i_L\mathcal{G}(\omega_4+\omega_3-\omega_2+\omega_1) \mu^j_L\mathcal{G}(\omega_3-\omega_2+\omega_1)\mu^k_L\mathcal{G}(-\omega_2+\omega_1)\mu^l_R\mathcal{G}(\omega_1)\mu^m_L\rangle, \quad [38]$$

$$S_b^{(4)}(\omega,T) = -\frac{2}{\hbar^5}\mathrm{Im}\int\frac{d\omega_4}{2\pi}\frac{d\omega_3}{2\pi}\frac{d\omega_2}{2\pi}\frac{d\omega_1}{2\pi} \delta(\omega-\omega_4-\omega_3-\omega_2+\omega_1)I^{(5)}_{ijklm,abcde}E^{a*}_{\mathrm{LO}}(\omega)E^b_{\mathrm{x}}(\omega_4)E^c_{\mathrm{v}}(\omega_3) E^{d}_{\mathrm{p}}(\omega_2)E^{e,*}_{\mathrm{p}}(\omega_1)e^{-i(\omega_2-\omega_1)T}\times\langle\mu^i_L\mathcal{G}(\omega_4+\omega_3+\omega_2-\omega_1) \mu^j_L\mathcal{G}(\omega_3+\omega_2-\omega_1)\mu^k_L\mathcal{G}(\omega_2-\omega_1)\mu^l_R\mathcal{G}(-\omega_1)\mu^m_L\rangle. \quad [39]$$

The rotational averaging of rank 5 tensors is carried out by $I^{(5)}_{ijklm,abcde}$ (65). Unlike $I^{(3)}_{ijk,abc} = \frac{1}{6}\epsilon_{ijk}\epsilon_{abc}$ which is constructed from a single product, the $I^{(5)}_{ijklm,abcde}$ is made of 10 isomers:

$$I^{(5)}_{ijklm,abcde} = \frac{1}{30}\Big(\epsilon_{ijk}\delta_{lm}\epsilon_{abc}\delta_{de} + \epsilon_{ijl}\delta_{km}\epsilon_{abd}\delta_{ce} + \epsilon_{ijm}\delta_{kl}\epsilon_{abe}\delta_{cd} + \epsilon_{ikl}\delta_{jm}\epsilon_{acd}\delta_{be} + \epsilon_{ikm}\delta_{jl}\epsilon_{ace}\delta_{bd} + \epsilon_{ilm}\delta_{jk}\epsilon_{ade}\delta_{bc} + \epsilon_{jkl}\delta_{im}\epsilon_{bcd}\delta_{ae} + \epsilon_{jkm}\delta_{il}\epsilon_{bce}\delta_{ad} + \epsilon_{jlm}\delta_{ik}\epsilon_{bde}\delta_{ac} + \epsilon_{klm}\delta_{ij}\epsilon_{cde}\delta_{ab}\Big). \quad [40]$$

The 10 terms in $I^{(5)}_{ijklm,abcde}$ are not linearly independent and can be reduced to 6 using the irreducible tensor algebra (66). This means that signals of order $2n$ with $n > 1$ may not generally be recast as a simple overlap integral like $S^{(2)}_{\mathrm{SFG}}$, Eq. **13**, but rather as a sum of overlap integrals of the various matter and field rotational invariants. The coupling between the six linearly independent SO(3) invariants and the rotationally averaged sum-over states $\chi^{(4)}$ expressions can be explicitly analyzed using representation theory techniques. The SO(3) action on the space $V_1^{\otimes 5}$ of rank 5 tensors natural extends to the action of SO(3) × S_5, with the latter being the symmetric group of permutations of 5 objects. The aforementioned six-dimensional space of SO(3)-invariants can be viewed as the space of an irreducible representation of S_5, labeled by the Young tableaux (3,1,1). The diagonal coupling between the field and matter invariants is achieved via choosing an orthonormal basis set in the space of the (3,1,1) representation of S_5. This point will be addressed elsewhere.

In the $S_b^{(4)}(\omega, T)$ signal presented here, the first two interactions involve the same pulse $\boldsymbol{E}_p$, chosen to be linearly polarized. The polarization of pulses $\boldsymbol{E}_{\mathrm{v}}$, $\boldsymbol{E}_{\mathrm{x}}$, and $\boldsymbol{E}_{\mathrm{LO}}$ are chosen to be polarized along the z, y, and x axes, respectively. This greatly reduces the number of rotational invariants to three, obtained by the contraction with $(1/30)(\epsilon_{ijk}\delta_{lm}\epsilon_{abc}\delta_{de} + \epsilon_{jkl}\delta_{im}\epsilon_{bcd}\delta_{ae} + \epsilon_{jkm}\delta_{il}\epsilon_{bce}\delta_{ad})$. The corresponding field invariants are $\boldsymbol{E}_{\mathrm{LO}}\cdot(\boldsymbol{E}_{\mathrm{x}}\times\boldsymbol{E}_{\mathrm{v}})|\boldsymbol{E}_{\mathrm{p}}|^2$, $\boldsymbol{E}_{\mathrm{x}}\cdot(\boldsymbol{E}_{\mathrm{v}}\times\boldsymbol{E}^*_{\mathrm{p}})\boldsymbol{E}_{\mathrm{LO}}\cdot\boldsymbol{E}_{\mathrm{p}}$ and $\boldsymbol{E}_{\mathrm{x}}\cdot(\boldsymbol{E}_{\mathrm{v}}\times\boldsymbol{E}_{\mathrm{p}})\boldsymbol{E}_{\mathrm{LO}}\cdot\boldsymbol{E}^*_{\mathrm{p}}$. These field invariants are similar to the ones discussed by Ayuso et al. (24) and that they denote as $h^{(5)}$.

In the main text, Eqs. **38** and **39** can be further simplified using the following definitions:

$$\chi_F^{(4,a)}(\omega, T; \omega_4, \omega_3, \omega_2, \omega_1) = E_{\mathrm{LO}}^{a*}(\omega)E_{\mathrm{x}}^{b}(\omega_4)E_{\mathrm{v}}^{c}(\omega_3)$$
$$E_{\mathrm{p}}^{d,*}(\omega_2)E_{\mathrm{p}}^{e}(\omega_1)e^{i(\omega_2-\omega_1)T}\delta(\omega-\omega_4-\omega_3+\omega_2-\omega_1), \quad [41]$$

$$\chi_F^{(4,b)}(\omega, T; \omega_4, \omega_3, \omega_2, \omega_1) = E_{\mathrm{LO}}^{a*}(\omega)E_{\mathrm{x}}^{b}(\omega_4)E_{\mathrm{v}}^{c}(\omega_3)$$
$$E_{\mathrm{p}}^{d}(\omega_2)E_{\mathrm{p}}^{e,*}(\omega_1)e^{-i(\omega_2-\omega_1)T}\delta(\omega-\omega_4-\omega_3-\omega_2+\omega_1). \quad [42]$$

The matter chiral response functions are given by:

$$\chi_M^{(4,a)}(\omega_4, \omega_3, \omega_2, \omega_1) = \sum_{ee'fc} \mu_{e'c}^{i}\mu_{cf}^{j}\mu_{fe}^{k}\mu_{e'g}^{l}\mu_{eg}^{m}I_{ce'}(\omega_4+\omega_3-\omega_2$$
$$+\omega_1)I_{fe'}(\omega_3-\omega_2+\omega_1)I_{ee'}(-\omega_2+\omega_1)I_{eg}(\omega_1), \quad [43]$$

$$\chi_M^{(4,b)}(\omega_4, \omega_3, \omega_2, \omega_1) = \sum_{ee'fc} \mu_{e'c}^{i}\mu_{cf}^{j}\mu_{fe}^{k}\mu_{eg}^{l}\mu_{e'g}^{m}I_{ce'}(\omega_4+\omega_3$$
$$+\omega_2-\omega_1)I_{fe'}(\omega_3-\omega_2-\omega_1)I_{ee'}(\omega_2-\omega_1)I_{ge'}(-\omega_1), \quad [44]$$

where $I_{ab}(\omega) = 1/(\omega - \omega_{ab} + i\Gamma_{ab})$.

Data, Materials, and Software Availability. Mathematica notebook and transition dipoles data have been deposited in Zenodo (https://zenodo.org/records/11068977) (67). All other data are included in the main text.

ACKNOWLEDGMENTS. Work by J.R.R. and Y.N. was supported by the U.S. Department of Energy (DOE), Office of Science, Basic Energy Science (BES), Chemical Sciences, Geosciences and Biosciences Division, under Contract No. DE-AC02-06CH11357. S.M. gratefully acknowledges the support of the NSF through Grant No. CHE-2246379. V.Y.C. gratefully acknowledge the support of the US DOE, BES Award No. DESC0022134.

1. Y. Tang, A. E. Cohen, Optical chirality and its interaction with matter. *Phys. Rev. Lett.* **104**, 163901 (2010).
2. Y. Tang, A. E. Cohen, Enhanced enantioselectivity in excitation of chiral molecules by superchiral light. *Science* **332**, 333–336 (2011).
3. D. M. Lipkin, Existence of a new conservation law in electromagnetic theory. *J. Math. Phys.* **5**, 696–700 (1964).
4. J. R. Rouxel, V. Y. Chernyak, S. Mukamel, Non-local real-space analysis of chiral optical signals. *Chem. Sci.* **7**, 6824–6831 (2016).
5. D. Ayuso, A. F. Ordonez, O. Smirnova, Ultrafast chirality: The road to efficient chiral measurements. *Phys. Chem. Chem. Phys.* **24**, 26962–26991 (2022).
6. M. Schmid *et al.*, Unveiling excited-state chirality of binaphthols by femtosecond circular dichroism and quantum chemical calculations. *J. Phys. Chem. Lett.* **10**, 4089–4094 (2019).
7. M. Oppermann *et al.*, Ultrafast broadband circular dichroism in the deep ultraviolet. *Optica* **6**, 56–60 (2019).
8. J. R. Rouxel, S. Mukamel, Molecular chirality and its monitoring by ultrafast X-ray pulses. *Chem. Rev.* **122**, 16802–16838 (2022).
9. Y. R. Shen, *The Principles of Nonlinear Optics* (Wiley, New York, 1984).
10. Y. Shen, Surface properties probed by second-harmonic and sum-frequency generation. *Nature* **337**, 519–525 (1989).
11. Y. Nagata, S. Mukamel, Vibrational sum-frequency generation spectroscopy at the water/lipid interface: Molecular dynamics simulation study. *J. Am. Chem. Soc.* **132**, 6434–6442 (2010).
12. P. Rentzepis, J. Giordmaine, K. Wecht, Coherent optical mixing in optically active liquids. *Phys. Rev. Lett.* **16**, 792 (1966).
13. M. Belkin, T. Kulakov, K. H. Ernst, L. Yan, Y. Shen, Sum-frequency vibrational spectroscopy on chiral liquids: A novel technique to probe molecular chirality. *Phys. Rev. Lett.* **85**, 4474 (2000).
14. P. Fischer, D. S. Wiersma, R. Righini, B. Champagne, A. D. Buckingham, Three-wave mixing in chiral liquids. *Phys. Rev. Lett.* **85**, 4253 (2000).
15. P. Fischer, F. Hache, Nonlinear optical spectroscopy of chiral molecules. *Chirality Biol. Chem. Conseq. Mol. Asymm.* **17**, 421–437 (2005).
16. A. Shkurinov, A. Dubrovskii, N. Koroteev, Second harmonic generation in an optically active liquid: Experimental observation of a fourth-order optical nonlinearity due to molecular chirality. *Phys. Rev. Lett.* **70**, 1085 (1993).
17. N. I. Koroteev, "Novel non-linear optical techniques for studying chiral molecules" in *Frontiers in Nonlinear Optics, The Sergei Akhmanov Memorial Volume*, Taylor & Francis, Ed. (CRC Press, 2021), p. 228.
18. B. Busson, A. Tadjeddine, Chiral specificity of doubly resonant sum-frequency generation in an anisotropic thin film. *J. Phys. Chem. C* **112**, 11813–11821 (2008).
19. P. Fischer, K. Beckwitt, F. Wise, A. Albrecht, The chiral specificity of sum-frequency generation in solutions. *Chem. Phys. Lett.* **352**, 463–468 (2002).
20. P. E. Schipper, On the induction of optical activity in achiral molecules. *Mol. Phys.* **29**, 1705–1716 (1975).
21. S. Yamaguchi, K. Shiratori, A. Morita, T. Tahara, Electric quadrupole contribution to the nonresonant background of sum frequency generation at air/liquid interfaces. *J. Chem. Phys.* **134** (2011).
22. M. Belkin, S. Han, X. Wei, Y. Shen, Sum-frequency generation in chiral liquids near electronic resonance. *Phys. Rev. Lett.* **87**, 113001 (2001).
23. R. Cireasa *et al.*, Probing molecular chirality on a sub-femtosecond timescale. *Nat. Phys.* **11**, 654–658 (2015).
24. D. Ayuso *et al.*, Synthetic chiral light for efficient control of chiral light–matter interaction. *Nat. Photonics* **13**, 866–871 (2019).
25. A. F. Ordonez, O. Smirnova, Generalized perspective on chiral measurements without magnetic interactions. *Phys. Rev. A* **98**, 063428 (2018).
26. D. Ayuso, P. Decleva, S. Patchkovskii, O. Smirnova, Chiral dichroism in bi-elliptical high-order harmonic generation. *J. Phys. B: Atomic, Mol. Opt. Phys.* **51**, 06LT01 (2018).
27. D. Baykusheva, M. S. Ahsan, N. Lin, H. J. Wörner, Bicircular high-harmonic spectroscopy reveals dynamical symmetries of atoms and molecules. *Phys. Rev. Lett.* **116**, 123001 (2016).
28. D. Baykusheva, H. J. Wörner, Chiral discrimination through bielliptical high-harmonic spectroscopy. *Phys. Rev. X* **8**, 031060 (2018).
29. D. Baykusheva *et al.*, Real-time probing of chirality during a chemical reaction. *Proc. Natl. Acad. Sci. U.S.A.* **116**, 23923–23929 (2019).
30. C. Cohen-Tannoudji, J. Dupont-Roc, G. Grynberg, *Photons and Atoms - Introduction to Quantum Electrodynamics* (Wiley, Berlin, 1997).
31. S. Mukamel, *Principles of Nonlinear Optical Spectroscopy* (Oxford University Press, Oxford, 1995).
32. G. Richmond, Molecular bonding and interactions at aqueous surfaces as probed by vibrational sum frequency spectroscopy. *Chem. Rev.* **102**, 2693–2724 (2002).
33. M. Bogle, J. Hearst, V. Jones, L. Stoilov, Lissajous knots. *J. Knot Theory Its Ramifications* **3**, 121–140 (1994).
34. D. Creed, The photophysics and photochemistry of the near-UV absorbing amino acids–I. Tryptophan and its simple derivatives. *Photochem. Photobiol.* **39**, 537–562 (1984).
35. N. S. Babcock *et al.*, Ultraviolet superradiance from mega-networks of tryptophan in biological architectures. *J. Phys. Chem. B* **128**, 4035–4046 (2024).
36. H. J. Werner et al., A general-purpose quantum chemistry program package. *Wiley Interdiscip. Rev.: Comput. Mol. Sci.* **2**, 242–253 (2012).
37. S. Mohan, N. Puviarasan, S. Bakkialakshmi, Vibrational spectra and analysis of tryptophan. *Asian J. Chem.* **11**, 1137 (1999).
38. U. Harbola, S. Mukamel, Coherent stimulated X-ray Raman spectroscopy: Attosecond extension of resonant inelastic X-ray Raman scattering. *Phys. Rev. B* **79**, 085108 (2009).
39. J. T. O'Neal *et al.*, Electronic population transfer via impulsive stimulated X-ray Raman scattering with attosecond soft-X-ray pulses. *Phys. Rev. Lett.* **125**, 073203 (2020).
40. K. Bennett, Y. Zhang, M. Kowalewski, W. Hua, S. Mukamel, Multidimensional resonant nonlinear spectroscopy with coherent broadband X-ray pulses. *Phys. Scr.* **2016**, 014002 (2016).
41. L. Young *et al.*, Roadmap of ultrafast X-ray atomic and molecular physics. *J. Phys. B: Atom. Mol. Opt. Phys.* **51**, 032003 (2018).
42. E. Schneidmiller *et al.*, Two-color operation of a soft X-ray FEL with alternation of undulator tunes. *Appl. Sci.* **13**, 67 (2022).
43. I. Inoue, T. Osaka, T. Hara, M. Yabashi, Two-color X-ray free-electron laser consisting of broadband and narrowband beams. *J. Synchrot. Radiat.* **27**, 1720–1724 (2020).
44. M. Ilchen *et al.*, Opportunities for gas-phase science at short-wavelength free-electron lasers with undulator-based polarization control. arXiv [Preprint] (2023). https://arxiv.org/abs/2311.11519 (Accessed 1 February 2024).
45. E. Ferrari *et al.*, Free electron laser polarization control with interfering crossed polarized fields. *Phys. Rev. Accel. Beams* **22**, 080701 (2019).
46. T. E. Glover *et al.*, X-ray and optical wave mixing. *Nature* **488**, 603–608 (2012).
47. E. Shwartz, S. Shwartz, Difference-frequency generation of optical radiation from two-color X-ray pulses. *Opt. Expr.* **23**, 7471–7480 (2015).
48. J. R. Rouxel, M. Kowalewski, S. Mukamel, Diffraction-detected sum frequency generation: Novel ultrafast X-ray probe of molecular dynamics. *J. Phys. Chem. Lett.* **9**, 3392–3396 (2018).
49. D. Cho, J. R. Rouxel, M. Kowalewski, J. Lee, S. Mukamel, Imaging of transition charge densities involving carbon core excitations by all X-ray sum-frequency generation. *Philos. Trans. R. Soc. A* **377**, 20170470 (2019).
50. F. Weise, S. M. Weber, M. Plewicki, A. Lindinger, Application of phase, amplitude, and polarization shaped pulses for optimal control on molecules. *Chem. Phys.* **332**, 313–317 (2007).
51. L. Belshaw *et al.*, Observation of ultrafast charge migration in an amino acid. *J. Phys. Chem. Lett.* **3**, 3751–3754 (2012).
52. H. J. Wörner *et al.*, Charge migration and charge transfer in molecular systems. *Struct. Dyn.* **4**, 061508 (2017).
53. D. Cho, J. R. Rouxel, M. Kowalewski, J. Y. Lee, S. Mukamel, Attosecond X-ray diffraction triggered by core or valence ionization of a dipeptide. *J. Chem. Theory Comput.* **14**, 329–338 (2018).
54. A. S. Folorunso *et al.*, Attochemistry regulation of charge migration. *J. Phys. Chem. A* **127**, 1894–1900 (2023).
55. Y. Nam, J. R. Rouxel, J. Y. Lee, S. Mukamel, Monitoring aromatic ring-currents in mg-porphyrin by time-resolved circular dichroism. *Phys. Chem. Chem. Phys.* **22**, 26605–26613 (2020).
56. P. Fischer, Nonlinear optical spectroscopy of chiral molecules. *Compr. Chiropt. Spectrosc.: Instrum. Methodol. Theor. Simul.* **1**, 347–371 (2011).
57. L. D. Romero, S. Meech, D. Andrews, Five-wave mixing in molecular fluids. *J. Phys. B: Atom. Mol. Opt. Phys.* **30**, 5609 (1997).
58. S. Donskoi, V. Makarov, Five-wave mixing ωb= ω1+ ω1+ ω1- ω2 in the bulk of a chiral liquid. *J. Raman Spectrosc.* **31**, 779–784 (2000).
59. A. Villaeys, Y. J. Dappe, M. Zouari, H. Bouchriha, Time-delayed infrared-visible probe pulses in five-wave mixing spectroscopy. *Chem. Phys. Lett.* **358**, 130–138 (2002).

60. T. Brixner, G. Gerber, Femtosecond polarization pulse shaping. *Opt. Lett.* **26**, 557–559 (2001).
61. T. Brixner *et al*., Quantum control by ultrafast polarization shaping. *Phys. Rev. Lett.* **92**, 208301 (2004).
62. M. Sato *et al*., Terahertz polarization pulse shaping with arbitrary field control. *Nat. Photon.* **7**, 724–731 (2013).
63. B. J. Zhao *et al*., Infrared free induction decay (IR-FID) of non-interfacial origin observed in the interfacial sum-frequency generation vibrational spectroscopy (SFG-VS). *J. Phys. Chem. C* **128**, 1443–1456 (2024).
64. G. Perosa *et al*., Femtosecond polarization shaping of free-electron laser pulses. *Phys. Rev. Lett.* **131**, 045001 (2023).
65. D. P. Craig, T. Thirunamachandran, *Molecular Quantum Electrodynamics: An Introduction to Radiation–Molecule Interactions* (Courier Corporation, 1998).
66. J. R. Rouxel, A. Rajabi, S. Mukamel, Chiral four-wave mixing signals with circularly polarized X-ray pulses. *J. Chem. Theory Comput.* **16**, 5784–5791 (2020).
67. J. R. Rouxel *et al.*, Manipulating ultrafast even-order nonlinear chiral responses of L-tryptophan by polarization pulse shaping - Supporting Information. Zenodo. https://zenodo.org/records/11068977. Deposited 25 April 2024.